Larger and Steadier Warming since 1850 from Harmonized Land and Ocean Temperature Records

3

Duo Chan,[1]⇤ Geoffrey Gebbie,[2] Peter Huybers[3]

[1]School of Ocean and Earth Science, University of Southampton Waterfront Campus European Way, Southampton, SO14 3ZH, Hampshire, UK [2]Department of Physical Oceanography, Woods Hole Oceanographic Institution 360 Woods Hole Road, Woods Hole, 02543, Massachusetts, USA [3]Department of Earth and Planetary Sciences, Harvard University
20 Oxford Street, Cambridge, 02138, Massachusetts, USA

⇤To whom correspondence should be addressed; E-mail: Duo.Chan@soton.ac.uk

Larger and Steadier Warming since 1850 from Harmonized Land and Ocean Temperature Records

Duo Chan,[1*] Geoffrey Gebbie,[2] Peter Huybers[3]

[1]School of Ocean and Earth Science, University of Southampton
Waterfront Campus European Way, Southampton, SO14 3ZH, Hampshire, UK
[2]Department of Physical Oceanography, Woods Hole Oceanographic Institution
360 Woods Hole Road, Woods Hole, 02543, Massachusetts, USA
[3]Department of Earth and Planetary Sciences, Harvard University
20 Oxford Street, Cambridge, 02138, Massachusetts, USA
[*]To whom correspondence should be addressed; E-mail: Duo.Chan@soton.ac.uk

Accurate historical temperature estimates are crucial for understanding current warming levels and informing policy decisions. Trends in global land and ocean temperatures diverge, however, before 1945. Inter-calibration of coastal land-ocean temperatures indicates that this divergence arises from under-corrected biases in sea-surface temperature linked to late 19$^{\text{th}}$ century instrumentation changes. Harmonizing land and ocean temperatures yields a steadier warming since 1850, better aligning with reconstructions from proxies and results from models driven by external radiative forcing. Our estimates also suggest that the average temperature over 2019–2023 is 1.36°C warmer than the 1850–1900 baseline, or 10% higher than most existing estimates. 20-year average global mean temperatures are likely to exceed 1.5°C by 2028, regardless of emissions scenarios, though the likelihood of surpassing 2°C remains below 50% for scenarios with substantial emission reductions.

Introduction

Reconstructions of global mean surface temperature (GMST) are imperfect indicators of anthropogenic climate change. Temperature data are sparse for many regions, making the mean uncertain (*1*). Ocean temperatures are measured somewhat below the surface, and land temperatures two meters above the surface (*2, 3*). Nevertheless, surface temperature is unique in its mean values being plausibly reconstructed from instrumental records back to the 1850s. GMST is also a useful indicator of anthropogenic climate change because it relates to the elevation of the planet with which society most commonly interacts. For these reasons, GMST is widely used to summarize the climate state (*4, 5*) and figures prominently in policy goals seeking to mitigate overall warming.

The most recent five-year period (2019–2023) has been the warmest such interval in instrumental history in many GMST estimates. Estimates of the magnitude of this warming, however, differ by more than 0.2°C (*6–9*). The National Oceanic and Atmospheric Administration Global Temperature version 5 (NOAA Global Temperature 5) (*7*) estimates that the mean temperature for 2019–2023 was 1.12 [1.01, 1.21]°C, Goddard Institute for Space Studies Surface Temperature version 4 (GISTEMP4) (*8*) gives 1.17 [1.07, 1.23]°C, the Hadley Centre/Climatic Research Unit Temperature version 5 (HadCRUT5) (*6*) gives 1.25 [1.18, 1.33]°C, and Berkeley Earth (*9*) gives 1.35°C. Warming is computed relative to a 1850–1900 baseline, consistent with that used by the Intergovernmental Panel on Climate Change reports (*5*), except in the case of GISTEMP4, for which we use 1880–1900 because it starts in 1880. Uncertainties in brackets are reported as 95% confidence intervals unless otherwise specified, and confidence intervals are computed using ensemble estimates when available. The discrepancies among these warming estimates imply that the timing of surpassing 1.5°C is uncertain by as much as a decade (table S1).

A potentially important clue as to the source of discrepancies is the appearance of internal inconsistencies in GMST between sea surface temperatures (SSTs) and land surface air temperatures (LSATs). The most recent estimates of global LSAT from the Climate Research Unit Temperature version 5 (CRUTEM5) (*10*), GISTEMP4 land (*11*), and Berkeley Earth land (*12*) all indicate decadal variability that can be divided into three stages (Fig. 1A). When masked by the least common coverage across estimates (see methods), LSATs warm between 1850 and 1945 at an average rate of 0.06°C per decade, show almost no change from 1946 to 1975, and subsequently warm at 0.30°C per decade since 1976 (Table 1). In contrast, SSTs from the Hadley Centre SST version 4 (HadSST4) (*13*), the Extended Reconstructed SST version 5 (ERSST5) (*14*), and the Centennial Observation-Based Estimates of SST version 2 (COBESST2) (*15*) all indicate four stages (Fig. 1B). The masked mean global SSTs cool from 1850 to 1910 (on average -0.03°C per decade), warm from 1911 to 1945 (0.16°C per decade), and then have no change from 1945 to 1975 (0.00°C per decade) and subsequent warming (0.15°C per decade).

The discrepancies between LSAT and SST trends in the late 19$^{\mathrm{th}}$ and early 20$^{\mathrm{th}}$ centuries are difficult to reconcile, given the strong coupling between land and ocean surface temperatures. The basic expectation is for greenhouse-gas induced warming on land to exceed that over the ocean on account of land having smaller heat capacity and losing less heat through evaporation (*16*), however SSTs warm 0.03°C per decade faster than LSATs between 1910 and 1945. No such comparable differential land-sea warming rates are observed in simulations from the Coupled Model Intercomparison Phase 6 (CMIP6) (*17*). The reconstructed LSAT-SST relation is outside the range of 1683 forced simulations of the modern era (1850-2100) and 48 pre-industrial control simulations (Fig. 2A and Fig. S1). Thus, there is no analog to the observed LSAT-SST relation in more than 200,000 years of simulated climate. Also difficult to explain are reports that SSTs cooled at an average rate of 0.03°C per decade during the early epoch of 1850 to 1909, whereas LSATs warmed by 0.03°C per decade. Such a trend difference is similarly outside the range across forced and control simulations in CMIP6 (Fig. 2B).

Differences between historical LSAT and SST estimates indicate that either simulations show insufficient surface temperature heterogeneity (*18*) or that substantial errors exist in certain historical observations (*2, 19*). Although there is precedent for common biases appearing across model simulations (*20, 21*), we build on existing evidence for systematic differences between LSAT and SST observations (*22–24*) using a variety of recent results. Relationships between LSATs and SSTs are quantified using an ensemble of LSATs with discontinuities in temperature time series, also known as breakpoints, more comprehensively detected and removed (*25*) and a model of local ocean-atmosphere heat and radiative exchanges for comparing LSATs and SSTs along coastlines (*26*). Origins of potential data biases are examined using evidence from day-night temperature differences (*27, 28*) and physical models for bucket water temperatures (*29*). In addition, instrumentally-derived temperatures are checked using paleoclimate datasets (*30, 31*). After finding that each of these lines of evidence supports the presence of biases in existing 19$^{\mathrm{th}}$ century SST estimates, we present a bias-corrected estimate of GMST that indicates larger and steadier warming.

Results

Inconsistent Land and Ocean Temperatures Along Global Coasts

To explore the source of the divergence between historical LSAT and SST estimates, we examine their relative trends where they meet along coastlines. We use a recently-developed model of local ocean-atmosphere heat exchange and radiative anomalies to convert LSATs into SSTs (*26*). The model is empirically fit to observations since 1960 and then inverted to predict near-coast SSTs from LSATs (see methods). This approach resembles that of (*24*), who inferred SST corrections by linearly scaling LSATs using a globally uniform factor, but the model we use accounts for non-linear relationships between SSTs and LSATs and geographical variations in the coupling between air and sea temperatures (*26*).

We also leverage a recently-developed ensemble of LSATs for inferring SSTs. The LSAT ensemble builds on work (*32, 33*) to better identify and adjust for breakpoints in station records associated with moving stations, changing instruments, and urbanization (*25*). We use the LSAT ensemble to infer an ensemble of near-coast SSTs against which we compare ship-based SST observations. Note that accounting for breakpoints in station LSATs increases the estimated coastal LSAT trends by approximately 0.2°C/century (*34*) relative to the unhomogenized estimates used in (*24*).

LSAT-inferred SSTs near the coasts are consistent with observed coastal SSTs after 1946 but recapitulate the divergence between global-average LSATs and SSTs during earlier periods (Fig. 3A). Whereas observed coastal-mean SSTs show the same four trend epochs found in aforementioned global-scale SST estimates, inferred coastal SSTs show three epochs, consistent with both coastal and global-scale LSAT estimates. Between 1850 and 1900, the mean inferred SSTs along coasts are between 0.17 to 0.34°C cooler than existing SST estimates, but between 1901 and 1940, they are 0.00 to 0.18°C warmer. This result confirms substantial systematic biases in LSATs, SSTs, or both.

Remaining Biases in SST Estimates

There are several lines of evidence pointing to coastal LSAT-SST discrepancies being associated with a poorly documented shift from using more-insulated wooden to less-insulated canvas buckets for measuring SSTs in the late 19$^{\mathrm{th}}$ century (*35, 36*). The first piece of evidence comes from changes in the amplitude of the diurnal cycle. A less-insulated bucket tends to bias measured temperatures to show a larger amplitude diurnal cycle (*27, 29*) and overall cooler daily-average temperatures (*36–38*). The greater diurnal amplitude comes from additional daytime solar heating (*27*), and the overall cooling comes from wind-induced evaporative cooling that operates during both day and night (*36*). In tropical oceans (20°S–20°N), the amplitude of the diurnal cycle of ship-based SSTs measured relative to a modern climatology from drifting buoys increases from 0.05°C in the 1880s to 0.12°C in the early 1900s and then stabilizes around this value until the 1940s (Fig. 4A).

Both the trends in SST corrections and diurnal amplitudes indicate that a transition from wooden to canvas buckets was largely completed by 1900, earlier than an often assumed linear transition over 1870–1920 (*36, 39*). A similar correspondence between diurnal amplitude and LSAT-inferred SST corrections is found in higher latitudes during both winter and summer (Figs. S2, S3). During WWII, the diurnal amplitude dropped to values smaller than those measured by buoys, and the SST correction reversed sign (Fig. 4A). This change is consistent with a shift from bucket to engine-room-intake measurements (*40*) and the practice of reading nighttime temperature measurements indoors (*22*). Engine-room-intake samples have a smaller amplitude because they come from greater depth and are biased warm by the heat from ship engines (*27, 28*). Reading nighttime bucket SSTs indoors avoids detection but reduces the cold nighttime SST bias and the diurnal amplitude because buckets are exposed to warmer and less windy indoor environments (*28*).

The observed relationship between diurnal amplitude anomalies and temperature corrections is readily reproduced by a physical bucket model (*29*). Using previously-published parameters representing a wooden bucket, a large canvas bucket, and a small canvas bucket (*36*), the model reproduces the relationship between observed diurnal amplitudes and the discrepancy between inferred coastal SSTs and observed SSTs since the 1880s by imposing a transition from wooden to canvas buckets between 1880 and 1900 (Figs. 4B, S2, S3). Note that getting the timing of the transition in bucket measurement techniques correct is important because, for example, a small canvas bucket can be as much as half a degree Celsius cooler, on average, than a wooden bucket (*36*).

A New Sea Surface Temperature Estimate

Given evidence for under-corrected SST biases, we correct observational SSTs to be consistent with LSAT-inferred coastal SSTs. Our correction technique uses patterns derived from bucket models that connect coastal and interior ocean SSTs (*41*) (also see methods), and we call our estimate Dynamically Consistent SST (DCSST). DCSST is 0.06 to 0.19 °C cooler than existing SST estimates over 1850 to 1900, and 0.03 to 0.14°C warmer over 1901 to 1940 (Fig. 1B). These differences are computed after masking all datasets to the least common coverage and computing anomalies relative to a 1982–2014 climatology and are similar to those found in our coastal analysis (Fig. 3). DCSST also shows a three-stage decadal variability that is consistent with global LSAT estimates (Fig. 1A, B), as expected given the assumptions built into our corrections.

To further check our SST estimate, we use coral proxies of SST variability based on δ^{18}O and Sr/Ca proxies. We select the 26 coral records from the PAGES2k (*30*) and the Iso2k (*31*) collections whose sample correlation with collocated instrumental SSTs since 1950 has an absolute value higher than 0.4 (Fig. 5A). These records are calibrated to units of degrees Celsius using the collocated instrumental SST data, but only between 1950 to 2000 in order to allow objective comparison during earlier periods (see methods). Upon averaging over grid boxes containing both proxy and instrumental records, these proxy-based temperatures indicate a steady warming from 1850 to 1940 that aligns more closely with DCSST than other estimates. HadSST4 and ERSST5 estimates are, respectively, 0.14 [0.06, 0.22]°C and 0.24 [0.13, 0.36]°C warmer than the proxy reconstruction between 1850 and 1900, and are 0.19 [0.07, 0.30]°C and 0.16 [0.05, 0.25]°C colder between 1901 and 1910 (Fig. 5B). These proxy results are robust to a variety of plausible methodological differences, including using different correlation cutoffs for proxy selection, calibration intervals, and comparing against only Sr/Ca or δ^{18}O records (fig. S4). None of the instrumental or coral estimates that we consider suggest as much warming as found in a recent estimate derived from six Caribbean sclerosponges (*42*).

A New Combined Land and Ocean Temperature Estimate

Our LSAT and SST estimates are combined to produce an ensemble of GMST estimates that features consistent land and ocean temperatures and provides a comprehensive estimate of uncertainty. This ensemble is called the Dynamically Consistent ENsemble of Temperature (DCENT (*41*); also see methods). We first compare DCENT against existing estimates by averaging across those regions that are sampled in common by all datasets (Fig. 6A). Whereas the spatial averages across existing observations in existing datasets indicate cooling from 1850–1909, DCENT indicates weak warming at a rate of 0.03 [-0.01, 0.08]°C per decade, such that DCENT has a three, rather than four-stage, overall warming pattern. Similar to existing estimates, the warmest five-year interval on record is still 2019–2023 in DCENT, but the magnitude of warming is 1.25 [1.14, 1.34]°C. This central estimate is 0.06°C higher than HadCRUT5, 0.16°C higher than NOAA Global Temperature 5, 0.10°C higher than GISTEMP4, and 0.06°C higher than the Berkeley Earth estimate (Fig. 6E). DCENT thus shows a steadier and larger warming since 1850 than existing estimates.

Forming spatially-complete estimates of GMST is challenging because of the sparse sampling of most land, high-latitude, and Pacific regions during the late 19$^{\mathrm{th}}$ century (Fig. 6B). Another ambiguity is the definition of the surface in regions with sea ice, where the surface ocean or surface air may be chosen (*6, 9*). We estimate the bias and uncertainty associated with missing data using both definitions of the surface by comparing complete and subsampled spatial fields from CMIP6 simulations (see methods). Our estimate of sampling bias increases the 2019–2023 warming level by 0.04 [-0.03, 0.09]°C (fig. S5A), and using air temperature anomalies over sea ice increases the warming level by a further 0.08 [0.03, 0.14]°C (fig. S5B). The combined effect increases GMST warming by 0.11 [0.02, 0.22]°C, leading to the 2019–2023 warming level in DCENT being 1.36 [1.22, 1.49]°C relative to the 1850–1900 baseline (Fig. 6D&E).

Our estimate based on DCENT indicates ∼10% more warming than HadCRUT5, NOAA Global Temperature 5, and GISTEMP4 (Fig. 6E). DCENT warming is consistent with the 1.35 °C warming reported by Berkeley Earth (*9*), though this numerical consistency arises for different physical reasons. The greater warming in DCENT comes primarily from enforcing land-ocean consistency, whereas the higher warming rate in Berkeley Earth comes primarily from their inference of a higher rate of warming over sea ice (Fig. 6B&C). Berkeley Earth estimate that air temperature above Arctic sea ice warmed by 2.55°C between 1850-1900 and 2019-2023 and, thereby, contributed an additional 0.14°C to GMST warming (*9*) (fig. S5D). This sea-ice-warming estimate is on the upper end of our estimate of 0.08 [0.03, 0.14]°C derived from CMIP6 models and is higher than used in other infilled observational estimates (Fig. 6E).

Implications of DCENT

The pattern of warming in DCENT is readily explained by estimates of external radiative forcing (*43*), as illustrated using a simple two-box energy-balance model (EBM). The EBM has accounted for ocean heat uptake and is fitted to each temperature estimate, including DCENT, HadCRUT5, NOAA Global Temperature 5, and Berkeley Earth temperature (see methods). Among these, DCENT shows the lowest root-mean-square error (RMSE) with the EBM-produced temperature pattern in response to radiative forcing (fig. S6). Notable is that both the EBM and DCENT indicate that the GMST warming between 1976 and 2023 is twice as fast as that between 1910 and 1945, whereas existing estimates indicate that recent warming is only 25% faster (Table 1). More generally, the closer correspondence between the EBM results and the

DCENT estimate implies less internal climate variability (*43*) and hence greater predictability of GMST from greenhouse gases.

The increased historical warming estimate in DCENT also suggests a higher climate sensitivity. Based on DCENT, the best estimate of the climate feedback parameter in the EBM is 1.34 [1.26, 1.42] W/°C/m^2. When using 3.7 W/m^2 as the radiative forcing of doubling CO_2 (*44*), such a feedback estimate translates into a climate sensitivity of 2.76 [2.61, 2.94]°C, compared with 2.28 [2.15, 2.43]°C if using HadCRUT5, 1.84 [1.71, 2.01]°C using NOAA Global Temperature 5, and 2.48 [2.34, 2.64]°C using the Berkeley Earth temperature estimate (fig. S6).

DCENT estimates also have implications for limiting GMST warming to under 1.5°C relative to preindustrial conditions, an aim of the 2015 Paris Agreement (*45*). HadCRUT5, GISTEMP4, and NOAA Global Temperature 5 indicate a greater than 50% likelihood that the slow-varying temperature background, characterized by 20-year mean GMST, will exceed 1.5°C by 2032, 2036, and 2040, respectively (table S1, see methods). DCENT indicates a 50% likelihood of surpassing 1.5°C by no later than 2028 across emissions scenarios considered in the IPCC's Assessment Report 6 (Fig. 7). Berkeley Earth's estimate implies the same threshold crossing time as DCENT, given their equivalent warming estimates. Note that these model-based projections do not account for the possibility of volcanic eruptions that could delay warming (*46*). Although 1.5°C of GMST warming is imminent, whether warming will exceed 2°C still depends upon emissions scenarios. The high-emissions scenario, IPCC Shared Socioeconomic Pathway 5-8.5 (SSP5-8.5), gives a greater than 50% chance of exceeding 2.0°C at the beginning of the 2040s, whereas low emissions scenario, SSP1-1.9, gives a 85% chance of keeping warming below 2.0°C through 2100 (Fig. 7B).

Discussion

In this study, we combined coastal temperature comparisons, changes in the amplitude of diurnal cycles, and physical modeling of bucket water temperatures to detect and confirm under-corrected biases in historical sea surface temperature archives due to changing instrumentation in the late 19$^{\text{th}}$ century. It is probably unsurprising that existing SST estimates prior to the 1940s are uncertain. The HadSST4 estimate uses a physical bucket model to compute and remove biases between measured bucket water temperatures and actual SSTs (*13*), but key model parameters, such as bucket geometry and on-deck time, are poorly documented and inevitably uncertain (*36*). ERSST5 corrections make use of nighttime marine air temperatures (NMATs) (*14, 47*), but these are subject to biases associated with increasing ship height (*48*), wartime practices of reading temperatures inside ships (*22, 28*), and a data truncation bias during digitization that may similarly affect NMATs as it does SSTs (*49*).

Corrections to SST observations have generally relied upon physical models of temperature bias (*13–15, 36, 39, 47*). Using near-coast air temperature to correct SSTs was undertaken by ref. (*23*) in 1986, however, and revisited by ref. (*24*) in 2018. Our study builds upon these prior near-coast estimates to provide a new surface temperature ensemble wherein SSTs align with LSATs. In developing this ensemble we call upon better-homogenized coastal LSATs (*25*), physical models relating LSATs to SSTs (*26*), and additional lines of evidence involving the diurnal cycle, bucket modeling, and paleo-proxies.

Our estimate, DCENT, gives larger and steadier warming, consistent with both paleo-proxies and expectations from external radiative forcing. The reconciliation of instrumental records, paleo proxies, and physical expectations increases our confidence in the estimate of the current warming level. We find that warming is more likely than not to surpass 1.5°C by 2028, regardless of the emissions scenarios, or 3–4 years earlier than the IPCC estimated time frame (*5*).

This finding emphasizes the need to prepare for 2.0°C and higher warming thresholds while still highlighting the urgency of substantial emission reductions.

Materials and Methods

Dynamically Consistent Ensemble of Temperature (DCENT)

DCENT is a 200-member ensemble of monthly surface temperature estimates since 1850, provided at a resolution of $5^\circ \times 5^\circ$ (*41*). The development of DCENT involves five steps designed to address data challenges in both land surface air temperature (LSAT) and sea surface temperature (SST) records.

First, the land component (DCLSAT) is developed by homogenizing station temperatures using two improved pairwise homogenization algorithms that better account for autocorrelation in climate signals (*25*). These algorithms improve upon previous work (*34*) in identifying and adjusting for discontinuities in station records associated with changes in station locations and instruments, as well as urbanization (*25*). Each algorithm has its parameters perturbed 50 times, giving, in total, a 100-member ensemble (*25*). To further address data sparsity before 1900, we run the algorithms a second time on the original 100-member ensemble, focusing on stations before 1900. The ensemble after this additional step is pooled together with the original ensemble to create the 200-member DCLSAT ensemble (*41*).

Second, the DCLSAT ensemble is combined with a land-ocean energy-balance model (*26*) to infer coastal SSTs,

$$\frac{d\mathrm{SST}'}{dt} = \alpha \frac{d\mathrm{LSAT}'}{dt} - \beta \mathrm{SST}' + \gamma \mathrm{LSAT}', \tag{1}$$

wherein the change in near-coast SSTs is estimated from LSAT and SST anomalies in the current month. The parameters α, β, and γ are estimated empirically using high-quality data from after the 1960s before being applied to infer near-coast SSTs throughout the historical period (*26*). This model gives accurate predictions of SSTs based on local LSATs using both withheld observational data and historical simulations (*26*). An assumption of approximate stationarity of parameters during the historical period is supported by examination of model simulations (*26*). Our approach shares some features in common with ref. (*24*), who inferred SST corrections by linearly scaling LSATs using a globally uniform factor; however, our model accounts for non-linear relationships between SSTs and LSATs, as well as geographic variations in the coupling between air and sea temperatures (*26*).

Third, we apply a group-wise intercomparison algorithm to estimate and adjust systematic offsets among groups of ship-based SST measurements from ICOADS3.0.0 and 3.0.2 (*50*). ICOADS3.0.0 spans from 1850 to 2014, and ICOADS3.0.2 from 2015 to 2023. There exist systematic offsets among different groups of SSTs (*49, 51*). We follow a methodology detailed in ref. (*41*) that relies on physically simulated patterns of bucket biases to provide a set of seasonally varying spatial bases that are used to estimate and adjust group-wise offsets.

Fourth, because the group-wise intercomparison in step three does not address SST biases common to all groups, LSAT-inferred near-coast SSTs are used to further correct group-wise homogenized SSTs. Simulated patterns of bucket SST biases are matched using ordinary least squares against residuals between LSAT-inferred SSTs and group-wise homogenized SSTs. The fitted coefficients are then multiplied by simulated patterns of bucket biases and applied to further correct SSTs globally (*41*). The limited coastal data coverage before 1880 prevents a reliable estimate of common SST biases (*26*). We, therefore, follow a practice adopted by other SST products (*14, 52*) of using the estimated common bias in 1880 to adjust SSTs over 1850–1880 (*41*). Each member of the group-wise homogenized SSTs is referenced against a different member of the DCLSAT ensemble, resulting in a 200-member ensemble of SST estimates that we call dynamically consistent SST (DCSST).

Each realization of LSAT leads to an SST realization that is dynamically consistent. As a final step, members of DCLSAT are combined with their corresponding DCSST members to generate the full DCENT ensemble. Combined temperatures along coastal regions are weighted by the fraction of land and ocean area (*6*). Uncertainty is propagated across the multiple steps in developing DCENT for purposes of providing comprehensive uncertainty quantification. Differences in GMST warming between DCENT and existing estimates mainly arise from enforcing SSTs to be consistent with LSATs, as opposed to using a different set of LSAT estimates. In a sensitivity analysis where we use the homogenized GHCNmV4 LSAT dataset to infer and correct SSTs, we obtain a 2019–2023 masked mean temperature warming of 1.26°C relative to the 1850–1900 baseline that is nearly equivalent to the 1.25 [1.14, 1.34]°C estimate in DCENT.

Temperature estimates from other studies

There are four widely-used combined land and ocean temperature datasets against which we compare DCENT, each utilizing the most recent version available. These are the 200-member HadCRUT5 analysis ensemble (*6*), the 1000-member NOAA Global Temperature V5 ensemble (*7*), the 200-member GISTEMP4 ensemble (*8*), and the Berkeley Earth land-ocean temperature record (*9*). For HadCRUT5 analysis and Berkeley Earth temperature, we use the GMST time series from their providers. The NOAA Global Temperature V5 and the GISTEMP4 ensembles provide only gridded datasets, and we calculate a GMST from these datasets by weighting individual grid boxes using the cosine of latitudes. The Berkeley Earth temperature has two versions: one inferring under-sampled polar temperatures using air temperature anomalies over sea ice, and another using ocean temperature anomalies beneath sea ice. We examine both versions. The version involving air temperature over sea ice is used for reporting GMST statistics in the main text, and the difference between the two versions is used to quantify differences associated with the definition of GMST (see the "Sampling Uncertainty" section in Materials and Methods for a more detailed discussion).

With regard to SST estimates, comparisons are made against the 200-member HadSST4 ensemble (*13*), a 500-member ERSST5 ensemble (*14*), and COBESST2, which offers only a central estimate (*15*). Notably, HadSST4 is the SST component in both HadCRUT5 and the

Berkeley Earth land-ocean temperature, and ERSST5 is used in NOAA Global Temperature V5 and GISTEMP4. The HadSST4 ensemble accounts for uncertainties associated with bias corrections. To address additional uncertainties stemming from random measurement errors, ship-level biases, and insufficient temporal sampling, we perturb each member using uncertainty estimates provided in ref. (*13*). Details of this additional perturbation are described in section 2.2 of ref. (*26*). Furthermore, the ERSST5 ensemble consists of 1000 members from 1854 to 2016, but only 500 members from 2017 onward. Therefore, we use only the first 500 members in this study.

For LSATs, comparisons are made against the 200-member CRUTEM5 ensemble (*10*), GISTEMP4-land (*11*), and the Berkeley Earth land temperature product (*12*). The CRUTEM5 ensemble is constructed by subtracting the HadSST4 ensemble from the HadCRUT5 ensemble, while accounting for the ratio of land to ocean area. GISTEMP4-land, the land component of GISTEMP4, essentially represents a gridded and interpolated version of the homogenized Monthly Global Historical Climate Network version 4 (GHCNmV4) (*34*) — the land component of NOAA Global Temperature V5. Note that for purposes of intercomparison, trends are computed by averaging only across those grid boxes that contain data in all of the considered different products after regridding to a common $5° \times 5°$ basis, which we refer to as being masked by the least common coverage.

Earth System Model simulations

Simulated near-surface air temperature (CMIP output variable name "tas") and sea surface temperatures (CMIP6 output variable name "tos") are from the Coupled Model Intercomparison Project, Phase 6 (CMIP6) (*17*). These include the pre-industrial control experiment, the historical all-forcing experiment, and projections under a variety of plausible scenarios (details in table S2). Consistent with observational estimates, CMIP6 simulations are regridded to a common 5°×5° resolution.

Sampling Uncertainty

Accounting for regions not covered by DCENT is an important step in computing GMST. On the whole, regions with missing data have been inferred to have experienced greater warming such that spatial infilling leads to greater GMST warming (*53*). An important definitional choice also involves whether air temperature anomalies above or ocean temperature below are used for purposes of representing surface temperature in regions covered by sea ice, as mentioned earlier (*9*). The version of the Berkeley Earth temperature that uses air temperature anomalies over sea ice, for example, indicates 0.14°C higher warming than the version that uses water temperature anomalies beneath sea ice (*9*). We select a definition of GMST using air temperature anomalies over sea ice, following Berkeley Earth's recommendation (*9*).

Correction factors and their associated uncertainty for incomplete coverage and the use of air temperature anomalies over sea ice are estimated separately and combined for a final estimate of sampling uncertainty (fig. S5). For coverage effects, we calculate the difference between averages obtained with full coverage and after masking by minimum historical data coverage for each CMIP6 historical simulation (fig. S5A). Simulated surface temperatures are computed by combining tas over land and tos at the ocean surface for both open ocean and sea ice. The difference between using the full coverage and the masked mean gives a cooler 1850–1900 temperature baseline that increases the estimated 2019–2023 warming by 0.04 [-0.03, 0.09]°C. The uncertainty associated with correcting for incomplete coverage of annual temperatures generally decreases from 0.06 °C (1 standard error) in the 1850s to 0.02 °C in the 2010s, albeit with several localized maxima including several years after the opening of the Panama Canal in 1914 and during World War II (fig. S5A). This evolution of coverage uncertainty is consistent with estimates in ref. (*54*) (see their Fig. 6).

The effect of using air temperature over sea ice is estimated by calculating the difference between two versions of CMIP6 simulations with full coverage, one using air and the other using ocean temperature anomalies for sea-ice covered regions (fig. S5B). The differences suggest greater warming since the 1970s when using air temperatures, which further increases 2019–2023 temperature warming by 0.08 [0.03,0.14]°C. In comparison, the effect associated with using air temperature over sea ice is estimated to be 0.14°C in Berkeley Earth, which is at the 97.5$^{\mathrm{th}}$ percentile of our estimate based on CMIP6 simulations (fig. S5D). This larger sea-ice effect explains the greater difference between masked and infilled GMST warming seen in Fig. 6E for Berkeley Earth as compared to other products.

The combined effect of correcting for incomplete coverage and for using air temperature as opposed to sea surface temperature in regions of sea ice increases estimated GMST warming between 1850–1900 and 2019–2023 by 0.11 [0.02, 0.22]°C compared with using averages across only those regions containing observations. Our CMIP6-based estimates of the coverage uncertainty are statistically consistent with those from Berkeley Earth land-ocean temperatures (fig. S5C). Other instrumental estimates do not provide such a decomposition, but they all indicate that accounting for biases associated with missing data leads to a higher rate of historical warming relative to using masked data (fig. S5E).

Concatenating CMIP6 projections with historical observational estimates

We combine tas anomalies over land and sea ice and tos anomalies over the open ocean for temperature projections. To concatenate CMIP6 projections with observational estimates, which is crucial for quantifying the exceedance time of GMST, the sample mean value of the simulations over the years 2019–2023 is set equal to that of the observations over the same period. This approach ensures continuity across the observation-prediction boundary. Each simulation is paired randomly with a member of DCENT such that the spread in concatenated CMIP6 projections contains observational uncertainties, model spread, and simulated internal variability.

Paleo-proxies from corals

We use annually and sub-annually resolved coral δ^{18}O and Sr/Ca ratio records compiled under the 2017 version of the PAGES2k multi-proxy database (*30*) and the Iso2k v1.0.0 database (*31*). The seasonal cycle is removed from sub-annually resolved proxy records, after which anomalies are averaged to annual resolution in order to facilitate comparison. All proxies are then paired with individual instrumental temperature estimates at 5° resolution.

Comparisons are made according to the season indicated in the provided proxy metadata. If seasonality information is not available, coral-based proxies are assumed to indicate temperatures averaged over the entire calendar year. Only records that overlap with instrumental records for at least 30 years since 1910 are retained, reducing the number of records in the PAGES2k database from 196 to 69.

Proxy signals may be influenced by non-temperature factors, such as changes in water source properties or variations in salinity (*55*). To better ensure that each retained proxy record is indicative of temperature, proxy records are only retained if their Spearman's rank correlation (*56*) with collocated instrumental temperatures has an absolute value higher than 0.4. Note that proxy isotope measurements covary negatively with temperatures, and the coral records used in our analysis all have correlations with instrumental temperatures that are more negative than -0.4. Correlations are computed using overlapping data after 1950, and if more than one instrumental record exists, the averaged correlation is used to select proxies. This selection further reduces the number of proxies from 69 to 26, with 21 δ^{18}O and 5 Sr/Ca records. Using a threshold of 0.3 and 0.5 leads to, respectively, 35 and 17 proxies retained in the analysis, but where results are qualitatively consistent (fig. S4).

A total least squares approach (*57*) is used to calibrate proxies into temperature anomalies.

Specifically, we first linearly scale each proxy time series using the ratio of the 1950–2000 standard deviation between mean instrumental temperatures and the proxy. This approach is useful because both proxies and instrumental records contain uncertainties, whereas standard linear least-squares regression techniques would be susceptible to regression dilution (*57*). Coral-based records have their sign reversed to obtain a temperature scaling (fig. S7).

Diurnal cycle of SST

Diurnal SST anomalies are defined as SST anomalies relative to daily-mean values (*29*), which we calculate from individual ships on a daily basis using ICOADS3.0 data (*50*). Extracted diurnal anomalies are binned by local hour, month, and latitude, and the amplitude of the diurnal cycle is evaluated by fitting a once-per-day sinusoidal basis using least squares (*29*). Anomalous diurnal amplitudes are computed relative to collocated 1990–2014 climatological diurnal magnitudes estimated from drifting buoy SSTs (*51*). Note that buoy-based diurnal amplitude has shown very little change globally from 1980 to 2023 (<0.002°C per decade), which is much smaller compared to variations seen in ship-based measurements (fig. S8). As a result, it is reasonable to assume that the diurnal amplitude of SST is stable throughout the historical period.

Modeling water temperatures in buckets

A wooden bucket model is used to estimate biases in daily-average SST and the amplitude of the diurnal cycle. This model is an extension of ref. (*36*) and allows for simulating bucket biases at each local hour through improved schemes for solar heating (*29*). The model is driven using 1973–2002 monthly climatology of SST, 10-m air temperature, wind speed, and specific humidity from the National Oceanography Centre version 2.0 surface flux and meteorological dataset (*58*) and an insolation climatology from the ERA-Interim reanalysis (*59*).

The bucket model is run with different geometries to represent three types of buckets used in ref. (*36*): a wooden bucket with a diameter of 25 cm, a depth of 15 cm, and a thickness of 1 cm; a large canvas bucket with a diameter of 16.3 cm, a depth of 14 cm , and a thickness of 0.2 cm; and a small canvas bucket with a diameter of 8 cm, a depth of 12 cm, and a thickness of 0.2 cm. Except for bucket geometry, we use the same set of model parameters (see table S3). The use of a very-thin wooden bucket to represent the behavior of a canvas bucket is common practice (*29*).

Modeling GMST

A two-box energy-balance model (*60*) is used to simulate changes in temperature in response to changes in radiative forcing,

$$\begin{aligned} c_p \rho d_s \frac{dT_s}{dt} &= -\lambda T_s + F - \kappa (T_s - T_d), \\ c_p \rho d_d \frac{dT_d}{dt} &= \kappa (T_s - T_d), \end{aligned} \tag{2}$$

where T_s and T_d denotes temperatures in the surface and deep boxes, respectively. The term $c_p = 4180$ J/kg/°C is the heat capacity of sea water, and $\rho = 1030$ kg/m^3 is the sea water density. These two terms are multiplied by the effective depth of the surface (d_s) and deep boxes (d_d) to obtain the heat capacity of the corresponding boxes. The term λ denotes a climate feedback parameter, and κ is a ocean heat uptake coefficient. External radiative forcing from the year 1500, F, is prescribed according to ref. (*43*).

Bayesian inference is used to condition the parameters, d_s, d_d, λ, and κ, on 1850–2020 observational GMST estimates separately for each of the DCENT, HadCRUT5, NOAA global temperature V5, and the Berkeley Earth estimate, as well as on the 1960–2020 observational ocean heat content estimate from the Chinese Institute of Atmospheric Physics (*61*). Normal priors, $N(1, 0.5)$, that are truncated to be greater than zero are prescribed for λ and κ (in $W/^{\circ}C/m^2$), as well as $N(100, 50)$ for d_s and $N(1000, 500)$ for d_d (in m). Exponential priors with a mean of 1°C are prescribed for σ_s and with a mean of 1×10^{23}J for σ_d. The Bayesian modeling platform PyMC (*62*) is used to obtain the joint posterior distribution via Hamiltonian Markov Chain Monte Carlo and a No-U-Turn sampler (*63*).

References and Notes

1. C. P. Morice, J. J. Kennedy, N. A. Rayner and P. D. Jones. Quantifying uncertainties in global and regional temperature change using an ensemble of observational estimates: The HadCRUT4 data set, *Journal of Geophysical Research: Atmospheres* **117** (2012).

2. P. Jones. The reliability of global and hemispheric surface temperature records, *Advances in Atmospheric Sciences* **33**, pp. 269–282 (2016).

3. J. J. Kennedy. A review of uncertainty in in situ measurements and data sets of sea surface temperature, *Reviews of Geophysics* **52**, pp. 1–32 (2014).

4. S. K. Gulev, P. W. Thorne, J. Ahn, F. J. Dentener, C. M. Domingues, S. Gerland, D. Gong, D. S. Kaufman, H. C. Nnamchi, J. Quaas, J. A. Rivera, S. Sathyendranath, S. L. Smith, B. Trewin, K. von Shuckmann and R. S. Vose, *Climate Change 2021: The Physical Science Basis. Contribution of Working Group I to the Sixth Assessment Report of the Intergovernmental Panel on Climate Change* (Cambridge University Press, Cambridge, United Kingdom and New York, NY, USA, 2021), book section 2.

5. J. Y. Lee, J. Marotzke, G. Bala, L. Cao, S. Corti, J. P. Dunne, F. Engelbrecht, E. Fischer, J. C. Fyfe, C. Jones, A. Maycock, J. Mutemi, O. Ndiaye, S. Panickal and T. Zhou, *Climate Change 2021: The Physical Science Basis. Contribution of Working Group I to the Sixth Assessment Report of the Intergovernmental Panel on Climate Change* (Cambridge University Press, Cambridge, United Kingdom and New York, NY, USA, 2021), book section 4.

6. C. P. Morice, J. J. Kennedy, N. A. Rayner, J. Winn, E. Hogan, R. Killick, R. Dunn, T. Osborn, P. Jones and I. Simpson. An updated assessment of near-surface temperature change from 1850: The HadCRUT5 data set, *Journal of Geophysical Research: Atmospheres* **126**, pp. e2019JD032361 (2021).

7. B. Huang, M. J. Menne, T. Boyer, E. Freeman, B. E. Gleason, J. H. Lawrimore, C. Liu, J. J. Rennie, C. J. Schreck, F. Sun and others. Uncertainty estimates for sea surface temperature and land surface air temperature in NOAAGlobalTemp version 5, *Journal of Climate* **33**, pp. 1351–1379 (2020).

8. Nathan Lenssen and Gavin A. Schmidt and Michael Hendrickson and others. A NASA GISTEMPv4 Observational Uncertainty Ensemble, *ESS Open Archive* (2024). Available at ESS Open Archive.

9. R. A. Rohde and Z. Hausfather. The berkeley earth land/ocean temperature record, *Earth System Science Data* **12**, pp. 3469–3479 (2020).

10. T. J. Osborn, P. D. Jones, D. H. Lister, C. P. Morice, I. R. Simpson, J. Winn, E. Hogan and I. C. Harris. Land surface air temperature variations across the globe updated to 2019: The CRUTEM5 data set, *Journal of Geophysical Research: Atmospheres* **126**, pp. e2019JD032352 (2021).

11. N. J. Lenssen, G. A. Schmidt, J. E. Hansen, M. J. Menne, A. Persin, R. Ruedy and D. Zyss. Improvements in the GISTEMP uncertainty model, *Journal of Geophysical Research: Atmospheres* **124**, pp. 6307–6326 (2019).

12. R. Rohde, R. Muller, R. Jacobsen, E. Muller, S. Perlmutter, A. Rosenfeld, J. Wurtele, D. Groom and C. Wickham. A new estimate of the average Earth surface land temperature spanning 1753 to 2011., *Geoinformatics Geostatistics: An Overview, 1:1* (2013).

13. J. Kennedy, N. Rayner, C. Atkinson and R. Killick. An Ensemble Data Set of Sea Surface Temperature Change From 1850: The Met Office Hadley Centre HadSST. 4.0.0.0 Data Set, *Journal of Geophysical Research: Atmospheres* **124**, pp. 7719–7763 (2019).

14. B. Huang, P. W. Thorne, V. F. Banzon, T. Boyer, G. Chepurin, J. H. Lawrimore, M. J. Menne, T. M. Smith, R. S. Vose and H.-M. Zhang. Extended reconstructed sea surface temperature, version 5 (ERSSTv5): upgrades, validations, and intercomparisons, *Journal of Climate* **30**, pp. 8179–8205 (2017).

15. S. Hirahara, M. Ishii and Y. Fukuda. Centennial-scale sea surface temperature analysis and its uncertainty, *Journal of Climate* **27**, pp. 57–75 (2014).

16. S. Manabe, R. J. Stouffer, M. J. Spelman and K. Bryan. Transient responses of a coupled ocean–atmosphere model to gradual changes of atmospheric CO2. Part I. Annual mean response, *Journal of Climate* **4**, pp. 785–818 (1991).

17. V. Eyring, S. Bony, G. A. Meehl, C. A. Senior, B. Stevens, R. J. Stouffer and K. E. Taylor. Overview of the coupled model intercomparison project phase 6 (CMIP6) experimental design and organization, *Geoscientific Model Development* **9**, pp. 1937–1958 (2016).

18. T. Laepple and P. Huybers. Ocean surface temperature variability: Large model–data differences at decadal and longer periods, *Proceedings of the National Academy of Sciences* **111**, pp. 16682–16687 (2014).

19. E. C. Kent and J. J. Kennedy. Historical estimates of surface marine temperatures, *Annual Review of Marine Science* **13**, pp. 283–311 (2021).

20. C. K. Folland, O. Boucher, A. Colman and D. E. Parker. Causes of irregularities in trends of global mean surface temperature since the late 19th century, *Science Advances* **4**, pp. EAAO5297 (2018).

21. C. Wang, L. Zhang, S.-K. Lee, L. Wu and C. R. Mechoso. A global perspective on cmip5 climate model biases, *Nature Climate Change* **4**, pp. 201–205 (2014).

22. C. K. Folland, D. Parker and F. Kates. Worldwide marine temperature fluctuations 1856–1981, *Nature* **310**, pp. 670–673 (1984).

23. P. D. Jones, T. M. Wigley and P. B. Wright. Global temperature variations between 1861 and 1984, *Nature* **322**, pp. 430–434 (1986).

24. K. Cowtan, R. Rohde and Z. Hausfather. Evaluating biases in sea surface temperature records using coastal weather stations, *Quarterly Journal of the Royal Meteorological Society* **144**, pp. 670–681 (2018).

25. D. Chan, G. Gebbie and P. Huybers. An improved ensemble of land-surface air temperatures since 1880 using revised pair-wise homogenization algorithms accounting for autocorrelation, *Journal of Climate* (2024).

26. D. Chan, G. Gebbie and P. Huybers. Global and regional discrepancies between early 20th century coastal air and sea-surface temperature detected by a coupled energy-balance analysis, *Journal of Climate* **36**, pp. 2205–2220 (2023).

27. G. Carella, J. Kennedy, D. Berry, S. Hirahara, C. J. Merchant, S. Morak-Bozzo and E. Kent. Estimating sea surface temperature measurement methods using characteristic differences in the diurnal cycle, *Geophysical Research Letters* **45**, pp. 363–371 (2018).

28. D. Chan and P. Huybers. Correcting observational biases in sea surface temperature observations removes anomalous warmth during world war II, *Journal of Climate* **34**, pp. 4585–4602 (2021).

29. D. Chan and P. Huybers. Systematic differences in bucket sea surface temperatures caused by misclassification of engine room intake measurements, *Journal of Climate* **33**, pp. 7735–7753 (2020).

30. P. Consortium and others. A global multiproxy database for temperature reconstructions of the Common Era, *Scientific Data* **4** (2017).

31. B. L. Konecky, N. P. McKay, O. V. Churakova, L. Comas-Bru, E. P. Dassié, K. L. Delong, G. M. Falster, M. J. Fischer, M. D. Jones, L. Jonkers and others. The Iso2k database: a global compilation of paleo-δ 18 O and δ 2 H records to aid understanding of Common Era climate, *Earth System Science Data Discussions* **2020**, pp. 1–49 (2020).

32. M. J. Menne and C. N. Williams Jr. Homogenization of temperature series via pairwise comparisons, *Journal of Climate* **22**, pp. 1700–1717 (2009).

33. C. N. Williams, M. J. Menne and P. W. Thorne. Benchmarking the performance of pairwise homogenization of surface temperatures in the united states, *Journal of Geophysical Research: Atmospheres* **117** (2012).

34. M. J. Menne, C. N. Williams, B. E. Gleason, J. J. Rennie and J. H. Lawrimore. The global historical climatology network monthly temperature dataset, version 4, *Journal of Climate* **31**, pp. 9835–9854 (2018).

35. M. Bottomley, C. Folland, J. Hsiung, R. Newell and D. Parker. Global ocean surface temperature atlas (GOSTA), *Meteorological Office, Bracknell, UK* (1990).

36. C. Folland and D. Parker. Correction of instrumental biases in historical sea surface temperature data, *Quarterly Journal of the Royal Meteorological Society* **121**, pp. 319–367 (1995).

37. E. C. Kent, J. J. Kennedy, D. I. Berry and R. O. Smith. Effects of instrumentation changes on sea surface temperature measured in situ, *Wiley Interdisciplinary Reviews: Climate Change* **1**, pp. 718–728 (2010).

38. G. Carella, A. Morris, R. Pascal, M. Yelland, D. Berry, S. Morak-Bozzo, C. J. Merchant and E. Kent. Measurements and models of the temperature change of water samples in sea-surface temperature buckets, *Quarterly Journal of the Royal Meteorological Society* **143**, pp. 2198–2209 (2017).

39. J. Kennedy, N. Rayner, R. Smith, D. Parker and M. Saunby. Reassessing biases and other uncertainties in sea surface temperature observations measured in situ since 1850: 2. biases and homogenization, *Journal of Geophysical Research: Atmospheres* **116** (2011).

40. D. W. Thompson, J. J. Kennedy, J. M. Wallace and P. D. Jones. A large discontinuity in the mid-twentieth century in observed global-mean surface temperature, *Nature* **453**, pp. 646–649 (2008).

41. D. Chan, G. Geoffrey, P. Huybers and E. Kent. DCENT: Dynamicaly Consistent ENsemble of Temperature at the earth surface, *Scientific Data* pp. accepted (2024).

42. M. T. McCulloch, A. Winter, C. E. Sherman and J. A. Trotter. 300 years of sclerosponge thermometry shows global warming has exceeded 1.5°C, *Nature Climate Change* pp. 1–7 (2024).

43. K. Haustein, F. E. Otto, V. Venema, P. Jacobs, K. Cowtan, Z. Hausfather, R. G. Way, B. White, A. Subramanian and A. P. Schurer. A limited role for unforced internal variability in twentieth-century warming, *Journal of Climate* **32**, pp. 4893–4917 (2019).

44. Intergovernmental Panel on Climate Change, *Climate Change 2001: The Scientific Basis*, J. Houghton, Y. Ding, D. Griggs, M. Noguer, P. van der Linden, X. Dai, K. Maskell and

C. Johnson, eds. (Cambridge University Press, Cambridge, 2001), pp. 349–416. Contribution of Working Group I to the Third Assessment Report of the Intergovernmental Panel on Climate Change.

45. V. Masson-Delmotte, P. Zhai, H.-O. Pörtner, D. Roberts, J. Skea, P. R. Shukla, A. Pirani, W. Moufouma-Okia, C. Péan, R. Pidcock and others. Global warming of 1.5°C, *An IPCC Special Report on the impacts of global warming of* **1** (2018).

46. C. Timmreck. Modeling the climatic effects of large explosive volcanic eruptions, *Wiley Interdisciplinary Reviews: Climate Change* **3**, pp. 545–564 (2012).

47. T. M. Smith and R. W. Reynolds. Bias corrections for historical sea surface temperatures based on marine air temperatures, *Journal of Climate* **15**, pp. 73–87 (2002).

48. E. C. Kent, N. A. Rayner, D. I. Berry, M. Saunby, B. I. Moat, J. J. Kennedy and D. E. Parker. Global analysis of night marine air temperature and its uncertainty since 1880: The HadNMAT2 data set, *Journal of Geophysical Research: Atmospheres* **118**, pp. 1281–1298 (2013).

49. D. Chan, E. C. Kent, D. I. Berry and P. Huybers. Correcting datasets leads to more homogeneous early-twentieth-century sea surface warming, *Nature* **571**, pp. 393 (2019).

50. E. Freeman, S. D. Woodruff, S. J. Worley, S. J. Lubker, E. C. Kent, W. E. Angel, D. I. Berry, P. Brohan, R. Eastman, L. Gates and others. ICOADS Release 3.0: a major update to the historical marine climate record, *International Journal of Climatology* **37**, pp. 2211–2232 (2017).

51. D. Chan and P. Huybers. Systematic differences in bucket sea surface temperature measurements among nations identified using a linear-mixed-effect method, *Journal of Climate* **32**, pp. 2569–2589 (2019).

52. B. Huang, V. F. Banzon, E. Freeman, J. Lawrimore, W. Liu, T. C. Peterson, T. M. Smith, P. W. Thorne, S. D. Woodruff and H.-M. Zhang. Extended reconstructed sea surface temperature version 4 (ERSST. v4). Part I: Upgrades and intercomparisons, *Journal of Climate* **28**, pp. 911–930 (2015).

53. K. Cowtan and R. G. Way. Coverage bias in the hadcrut4 temperature series and its impact on recent temperature trends, *Quarterly Journal of the Royal Meteorological Society* **140**, pp. 1935–1944 (2014).

54. J. Kennedy, N. Rayner, R. Smith, D. Parker and M. Saunby. Reassessing biases and other uncertainties in sea surface temperature observations measured in situ since 1850: 1. measurement and sampling uncertainties, *Journal of Geophysical Research: Atmospheres* **116** (2011).

55. J.-E. Lee and I. Fung. "Amount effect" of water isotopes and quantitative analysis of post-condensation processes, *Hydrological Processes: An International Journal* **22**, pp. 1–8 (2008).

56. C. Spearman. Correlation calculated from faulty data, *British Journal of Psychology* **3**, pp. 271 (1910).

57. D. Chan, A. Rigden, J. Proctor, P. W. Chan and P. Huybers. Differences in radiative forcing, not sensitivity, explain differences in summertime land temperature variance change between CMIP5 and CMIP6, *Earth's Future* **10**, pp. e2021EF002402 (2022).

58. D. I. Berry and E. C. Kent. A new air–sea interaction gridded dataset from ICOADS with uncertainty estimates, *Bulletin of the American Meteorological Society* **90**, pp. 645–656 (2009).

59. D. Dee, S. Uppala, A. Simmons, P. Berrisford, P. Poli, S. Kobayashi, U. Andrae, M. Balmaseda, G. Balsamo, P. Bauer and others. The ERA-Interim reanalysis: Configuration and performance of the data assimilation system, *Quarterly Journal of the Royal Meteorological Society* **137**, pp. 553–597 (2011).

60. O. Geoffroy, D. Saint-Martin, D. J. Olivié, A. Voldoire, G. Bellon and S. Tytéca. Transient climate response in a two-layer energy-balance model. Part I: Analytical solution and parameter calibration using CMIP5 AOGCM experiments, *Journal of Climate* **26**, pp. 1841–1857 (2013).

61. L. Cheng, K. E. Trenberth, J. Fasullo, T. Boyer, J. Abraham and J. Zhu. Improved estimates of ocean heat content from 1960 to 2015, *Science Advances* **3**, pp. e1601545 (2017).

62. O. Abril-Pla, V. Andreani, C. Carroll, L. Dong, C. J. Fonnesbeck, M. Kochurov, R. Kumar, J. Lao, C. C. Luhmann, O. A. Martin and others. PyMC: a modern, and comprehensive probabilistic programming framework in Python, *PeerJ Computer Science* **9**, pp. e1516 (2023).

63. M. D. Hoffman, A. Gelman and others. The No-U-Turn sampler: adaptively setting path lengths in Hamiltonian Monte Carlo., *J. Mach. Learn. Res.* **15**, pp. 1593–1623 (2014).

64. Nathan Lenssen and Gavin A. Schmidt and Michael Hendrickson and others, Dataset for A NASA GISTEMPv4 Observational Uncertainty Ensemble, Google Drive dataset (2024). Accessed on June 20, 2024.

65. R. C. Gonzalez. Digital Image Processing. Pearson Education India (2009).

Acknowledgments: **Funding:** G.G. is supported by NSF OCE-2122805 and OCE-2103049. P.H. is supported by NSF Grant 2123295. **Authors contributions:** The authors designed the

study together; D.C. performed the analyses; and all authors contributed to interpreting results and writing the paper. **Competing interests:** The authors declare no competing interests. **Data and materials availability:** All datasets used in this study are publicly available as follows: HadSST4.0.2.0 200-member ensemble and uncertainty estimates (https://www.metoffice.gov.uk/hadobs/hadsst4), HadCRUT5.0.2.0 200-member ensemble and uncertainty estimates (https://www.metoffice.gov.uk/hadobs/hadcrut5), CRUTEM5.0.2.0 (https://www.metoffice.gov.uk/hadobs/crutem5), NOAA Global Temperature V5 ensemble (https://www.ncei.noaa.gov/pub/data/cmb/ersst/v5/2019.ngt.par/ensemble/), ERSST5 (https://www.ncei.noaa.gov/pub/data/cmb/ersst/v5/ensemble.1854-2017/ and https://www.ncei.noaa.gov/pub/data/cmb/ersst/v5/ensemble.2001.present/), GISTEMP4 land only estimate (https://data.giss.nasa.gov/pub/gistemp) and combined land-ocean temperature ensemble (*64*) (https://drive.google.com/drive/folders/1TptnbHgCQMpbPCweXccOLQPNoTcciGVi), Berkeley Earth land-ocean and land-only temperature (https://berkeleyearth.org/data/), COBESST2 (https://downloads.psl.noaa.gov/Datasets/COBE2), DCENT (https://doi.org/10.7910/DVN/NU4UGW), and monthly CMIP6 simulations (https://esgf-node.llnl.gov/search/cmip6). Code and data allowing the full reproduction of our results is publicly available with full access in a Harvard Dataverse Repository at https://doi.org/10.7910/DVN/UYJCVH.

Supplementary Materials

Figs. S1 to S8

Tables S1 to S3

Table 1: **Decadal trends (°C per decade) for LSAT, SST, and GMST estimates**. Note that GISTEMP4 starts in 1880 and trends are, thus, from 1880 rather than 1850. Note that trends reported over land or ocean separately are computed by averaging across only those grid boxes that contain observations in all considered products (i.e., masked by least common coverage across datasets), whereas GMST trends are corrected for lack of coverage (i.e., infilled, see Methods).

	1850-1909	**1910-1945**	**1850-1945**	**1946-1975**	**1976-2023**
LSAT (Masked by least common coverage across datasets)					
DCLSAT	0.06 [0.04, 0.07]	0.13 [0.12, 0.14]	0.08 [0.07, 0.09]	0.01 [0.00, 0.02]	0.30 [0.28, 0.30]
CRUTEM5	0.00 [-0.01, 0.03]	0.12 [0.07, 0.16]	0.04 [0.02, 0.06]	-0.01 [-0.02, 0.00]	0.30 [0.29, 0.31]
GISTEMP4	0.05	0.13	0.08	0.00	0.31
Berkeley	0.03	0.12	0.06	0.00	0.30
SST (Masked by least common coverage across datasets)					
DCSST	0.04 [-0.01, 0.09]	0.06 [0.04, 0.08]	0.04 [0.01, 0.06]	0.02 [0.01, 0.04]	0.14 [0.13, 0.15]
HadSST4	-0.03 [-0.05, -0.01]	0.16 [0.11, 0.21]	0.01 [-0.00, 0.03]	-0.02 [-0.07, 0.03]	0.15 [0.15, 0.15]
ERSST5	-0.05 [-0.08, -0.03]	0.16 [0.11, 0.20]	-0.00 [-0.02, 0.01]	0.02 [-0.01, 0.04]	0.14 [0.13, 0.15]
COBESST2	-0.02	0.15	0.02	-0.01	0.15
GMST (Infilled for global mean values)					
DCENT	0.03 [-0.01, 0.08]	0.09 [0.06, 0.12]	0.05 [0.02, 0.07]	0.03 [-0.01, 0.05]	0.19 [0.17, 0.20]
HadCRUT5	-0.02 [-0.04, 0.00]	0.16 [0.11, 0.19]	0.03 [0.01, 0.04]	-0.01 [-0.04, 0.03]	0.20 [0.19, 0.20]
NOAATEMP5	-0.04 [-0.05, -0.02]	0.14 [0.11, 0.18]	0.00 [-0.01, 0.02]	0.03 [-0.00, 0.05]	0.19 [0.18, 0.20]
GISTEMP4	-0.05 [-0.07, -0.02]	0.14 [0.10, 0.17]	0.04 [0.03, 0.05]	0.03 [0.01, 0.04]	0.19 [0.18, 0.20]
Berkeley	0.00	0.15	0.03	0.01	0.20

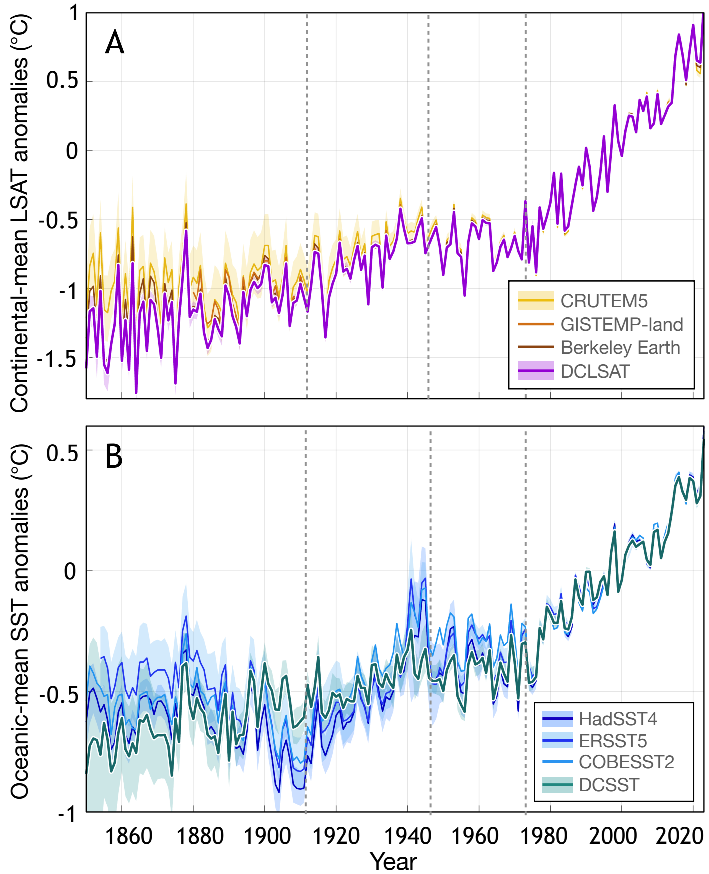

Fig. 1. Land and ocean temperatures. (**A**) Continental-mean land surface air temperature (LSAT) anomalies relative to a 1982–2014 mean for CRUTEM5 (light yellow), GISTEMP4 (dark yellow), Berkeley Earth (brown), and this study (DCLSAT, magenta). Shading denotes the 95% confidence interval where an ensemble is available. (**B**) as (A), but for oceanic-mean sea-surface temperature (SST) anomalies for HadSST4 (dark blue), ERSST5 (middle blue), COBESST2 (light blue), and this study (DCSST, green). Estimates are masked by their least common coverage before averaging.

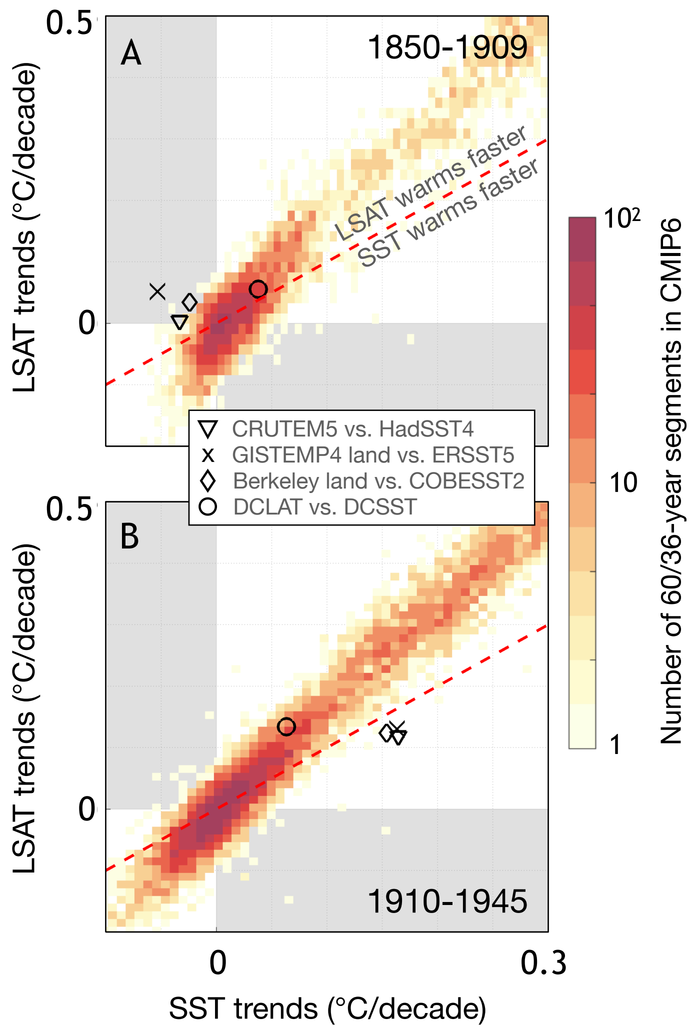

Fig. 2. LSAT and SST trends. (**A**) 60-year LSAT (y-axis) versus SST (x-axis) trends. Markers show the 1850–1909 observational trends, and the heatmap displays the histogram of trends in 60-year segments across CMIP6 historical, pi-Control, and all Shared Socioeconomic Pathway (SSP) scenario-based experiments. Note that Berkeley Earth used HadSST4 in their GMST estimate (*9*). Here, the Berkeley Earth estimate is plotted against COBESST2 simply for visualization purposes. (**B**) as (A), but for a 36-year analysis associated with the 1910–1945 trends.

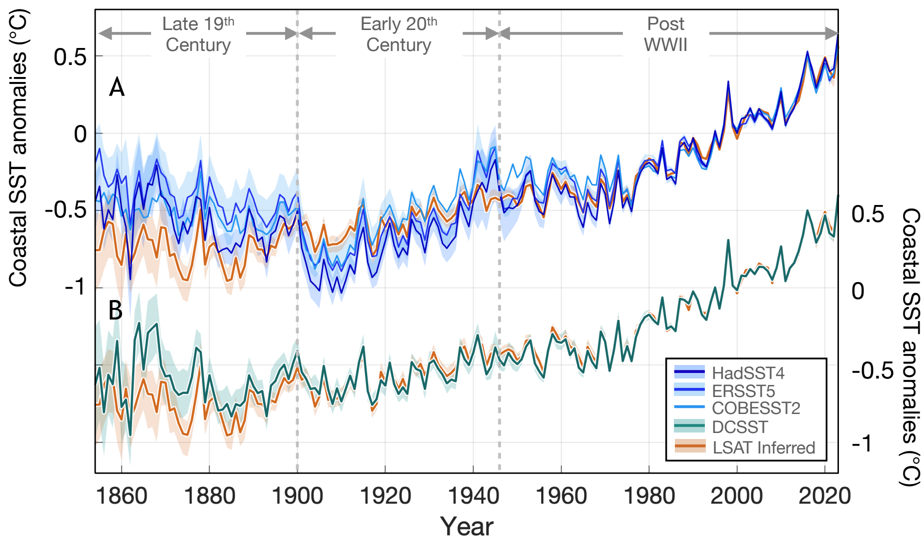

Fig. 3. Sea-surface temperatures averaged along global coasts. (**A**) Compared with the LSAT-inferred near-coast SST (orange), existing estimates, including HadSST4 (dark blue), ERSST5 (middle blue), and COBESST2 (light blue), each indicate significantly cooler coastal SSTs in the early 20th century and warmer SSTs in the late 19th century. Shown anomalies are relative to a 1982–2014 climatology, and shading denotes the 95% confidence interval. (**B**) as (A) but for coastal SSTs in DCSST (green) that are more consistent with SSTs inferred from coastal LSATs (orange).

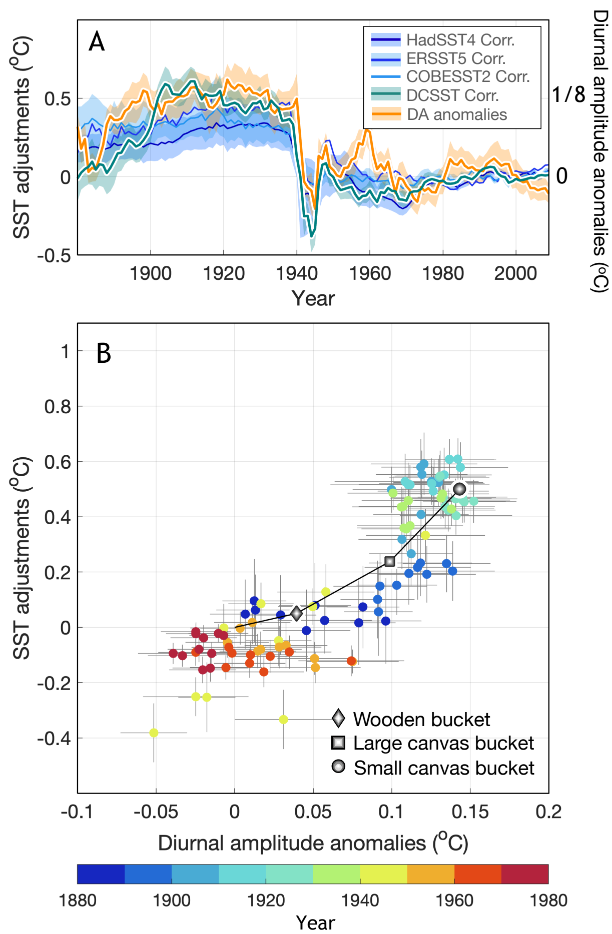

Fig. 4. Tropical SST correction and the amplitude of SST diurnal cycles. (**A**) Tropical (20°S-20°N) SST corrections relative to the 1982–2014 mean correction (left y-axis) in DCSST (green) and other SST estimates (blue). Also shown are anomalies in the amplitude of the diurnal cycle relative to a 1990–2014 climatology, estimated from drifting buoys (orange, right y-axis). (**B**) Tropical DCSST corrections (y-axis) versus anomalies in the diurnal cycle (x-axis) over 1880–1980 (colors of dots). Also shown are simulated daily mean bucket biases (y-axis) versus changes in the amplitude of diurnal cycles (x-axis) for a wooden bucket (diamond), a large canvas bucket (square), and a small canvas bucket (circle). The sign of simulated bucket biases is reversed to indicate required corrections. Errors, including shadings in (A) and bars in (B), represent 95% confidence intervals.

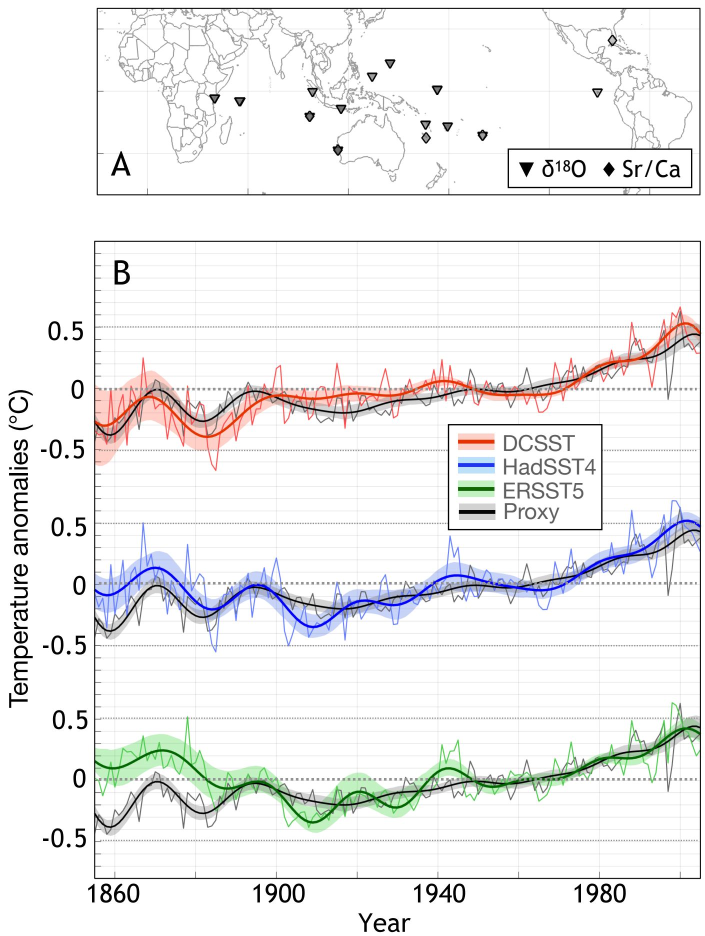

Fig. 5. Comparison with paleo-proxies. (**A**) annually or sub-annually resolved temperature-indicating coral records, including 21 δ^{18}O (downward triangle) and 5 Sr/Ca ratio (diamond) records. (**B**) Temperature anomalies from instrumental (color) and coral reconstructions (black) averaged over all sites where both instrumental and paleo-reconstructions are available. To highlight low-frequency variability, annual signals (light lines) are low-pass filtered (dark lines) using a Fourier filter (*65*) and a 1/(20 year) cutoff. Anomalies are shown relative to the average over 1930–1980. Shading denotes 95% confidence intervals for both instrumental and proxy records.

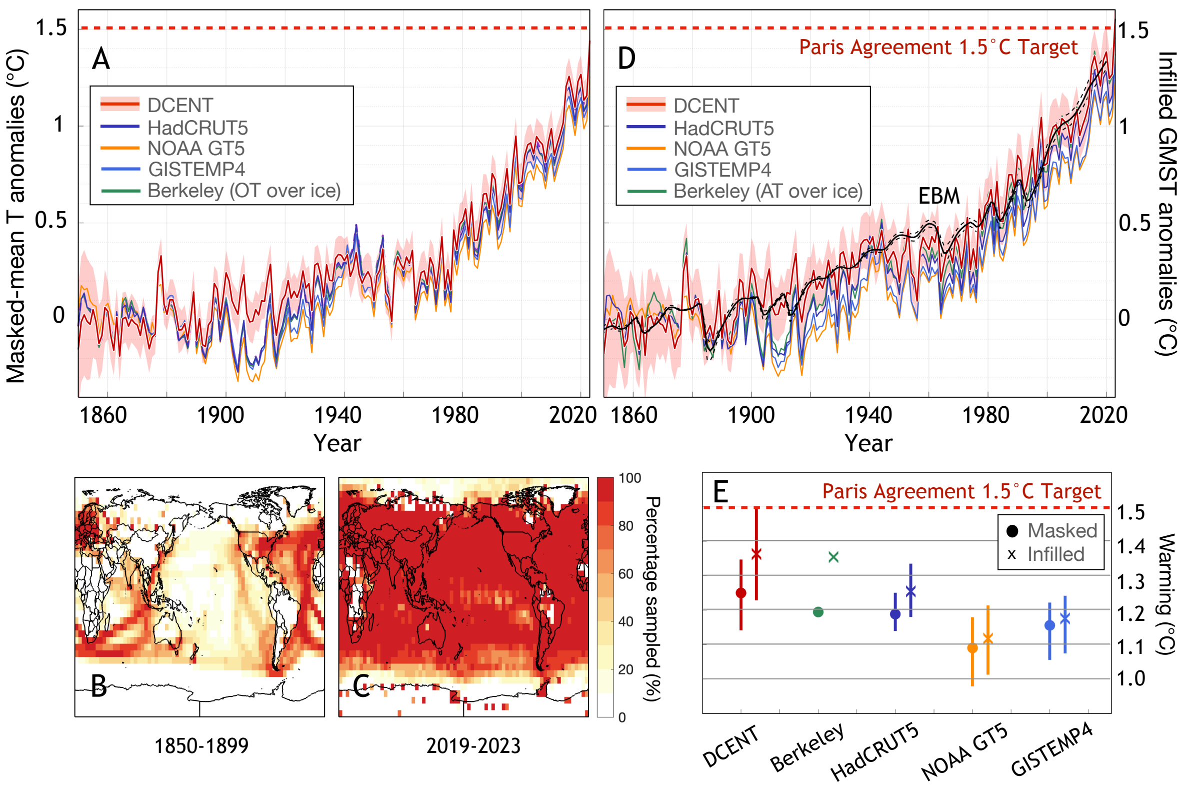

Fig. 6. Global Mean Surface Temperatures (GMST). (**A**) Mean temperature averaged over the least common coverage across datasets, including DCENT (red distribution), HadCRUT5 analysis (dark blue), NOAA Global Temperature 5 (orange), GISTEMP4 (light blue), and Berkeley Earth (green). (**B**) Percentage of monthly $5^\circ \times 5^\circ$ grid boxes sampled during 1850–1900. (**C**) as (B) but for 2019–2023. (**D**) as (A) but for infilled GMST estimates. Also shown is a simulation using a two-box energy-balance model (black), with model parameters fitted to DCENT using a Bayesian method (see methods). The 1.5°C warming level is highlighted with a dashed red line. (**E**) 2019–2023-mean GMST anomalies relative to the 1850–1900 baseline. Markers represent the central estimates for masked (circle) and infilled estimates (cross). Bars denote 95% confidence intervals. Note that GISTEMP4 data starts in 1880, and its statistics are computed relative to the mean over 1880–1900.

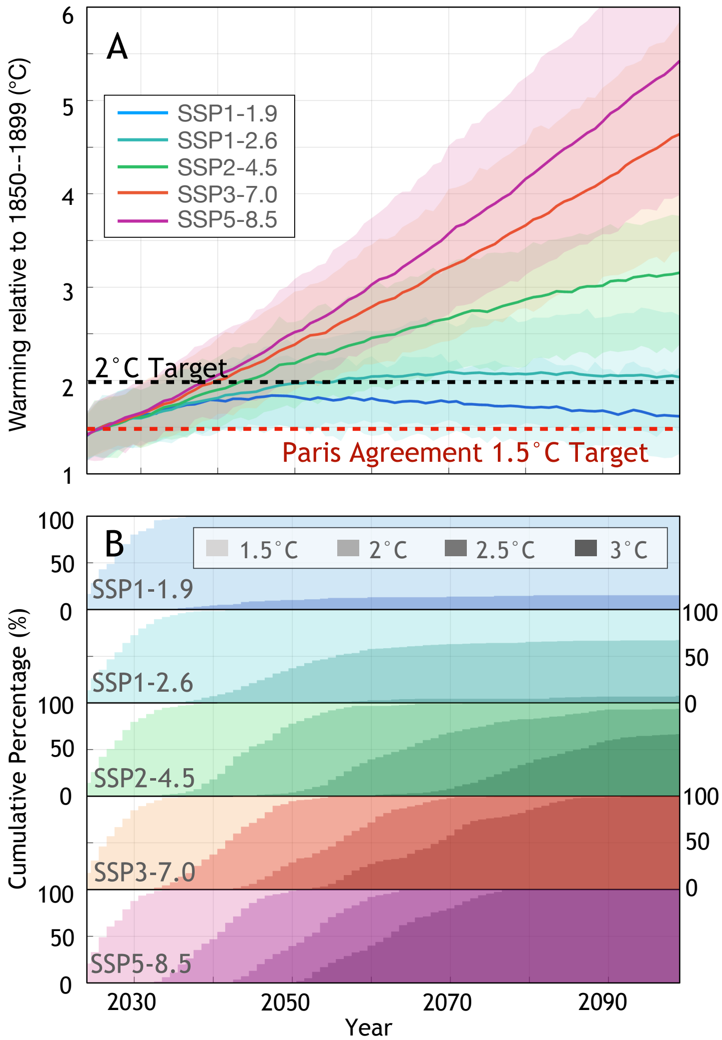

Fig. 7. Future GMST projections. (**A**) Projected GMST in different SSP scenarios, with shading showing corresponding 95% confidence intervals. Projections are concatenated with infilled GMST estimates from DCENT (see methods). (**B**) The cumulative percentage of projected 20-year mean GMST exceeding thresholds of 1.5, 2, 2.5, and 3°C threshold is, respectively, indicated by darker shading.